Numerical Reconstruction of Proton Exchange Membrane Fuel Cell Gas Diffusion Layers

ECS Transactions, 112 (4) 49-61 (2023)
10.1149/11204.0049ecst ©The Electrochemical Society

Numerical Reconstruction of Proton Exchange Membrane Fuel Cell Gas Diffusion Layers

D. Yang[a], H. Garg[a], S. B. Beale[b,c], and M. Andersson[a]

[a] Department of Energy Sciences, Lund University, 22100 Lund, Sweden
[b] Forschungszentrum Jülich GmbH, 52425 Jülich, Germany
[c] Department of Mechanical and Materials Engineering, Queen's University, Kingston ON K7L, 3N6, Canada

Stochastic reconstruction is widely employed for effective and flexible imitation of Gas Diffusion Layers (GDLs), e.g., to facilitate the study of their properties. However, the reconstruction often overlooks crucial factors such as fiber curvature, fiber stack arrangement, and fiber anisotropy. Consequently, the impact of these structural characteristics remains poorly understood. In this study, an in-house reconstruction procedure is developed based on the periodic surface model. This procedure enables the generation of GDLs with either straight or curved fibers, layer-by-layer or random arrangement, and different probabilities of through-plane fiber orientation angles. The porosity, domain size, and fiber diameter are extracted from an experimental image-based GDL and utilized as input data for the reconstruction. Furthermore, the different GDLs are compared in terms of pore size distribution and through-plane porosity distribution. It is concluded that introducing proper selections of these fiber features gives the reconstruction more realistic properties.

Introduction

A Proton Exchange Membrane Fuel Cell (PEMFC) is widely recognized as a clean and efficient power generation device, with zero pollution emissions. It holds significant promise for a diverse range of applications, including portable, stationary, and transportation sectors (1-3). One crucial component of the PEMFC is the Gas Diffusion Layer (GDL), typically composed of carbon fiber, additional binder, and hydrophobic agents like polytetrafluoroethylene (4, 5). The GDL performs several critical functions, such as providing mechanical support, facilitating gas transport, removing product water, and enabling thermal and electronic conduction. Accurate characterization of GDL transport properties is essential for improving fuel cell performance (5, 6).

Commercial GDLs are primarily made of carbon-based porous materials as well as minor metal-based materials. Various fabrication methods result in different GDL types, e.g., fiber paper, carbon cloth, carbon felt, and carbon foam (7). To characterize GDL structure properties, either experimental image-based (8-11) or stochastic geometry-based (12-14) reconstruction approaches are employed. Experimental images are typically obtained using advanced tools such as focused ion beam scanning electron microscope (8) or non-intrusive imaging techniques, e.g., microscale X-ray computed tomography (10).

Odaya et al. (11) adopted an X-ray computed tomography to effectively evaluate porosity distribution within the GDL. Both numerical and experimental methods are employed to investigate the impact of non-uniform compression (14, 15).

Stochastic methods involve cylindrical fiber generation with an appropriate diameter and a random distribution within a domain until the desired porosity is achieved. This approach offers advantages in terms of time and cost efficiency, as well as flexibility for structure optimization, such as incorporating additional components like binders and polytetrafluoroethylene (13, 16), and modifying fiber attributes like shape (17, 18), orientation (19), length, and diameter (20). However, most existing stochastic methods primarily focus on straight fibers, which are presented in carbon-paper-based GDLs (16-20), neglecting the presence of curved fibers commonly found in carbon felts and carbon cloth. The influence of layer-by-layer and random fiber stacking strategies on GDL properties remains unclear, and the consideration of GDL anisotropy is also limited.

This study aims to address these gaps by employing a theory of periodic surface model to numerically reconstruct GDLs containing both curved and straight fibers. A suitable range of fiber curvature is selected to investigate the effect of three different fiber layer stacking strategies and varying degrees of anisotropy. The utilized fiber diameter, porosity, and domain size are all extracted from an image-based GDL reconstruction and kept constant. The pore size distribution and local porosity distribution of the generated GDLs are analyzed.

Methodology

Periodic surface models

This work introduces a novel GDL reconstruction approach known as the periodic surface model, which is different from previous studies that generate straight fibers by randomly selecting two coordinate points in 3D space and constructing a straight cylindrical fiber between them (13). The periodic surface model, initially proposed by Wang (21) and further developed by Huang (22) with a generalized version, employs an iso-surface with distinctive shapes such as rods or spheres.

$$f(\boldsymbol{r}) = \sum_{l=1}^{L}\sum_{m=1}^{M}\mu_{lm}cos\left(2\pi k_l\left(\boldsymbol{P}_m^T\boldsymbol{r} + \sum_{s=1}^{S}\sum_{t=1}^{T}u_{lmst}cos\left(2\pi f_{lms}(\boldsymbol{Q}_{lmt}^T\boldsymbol{r})\right)\right)\right) = \psi_0 \quad [1]$$

Here, $\boldsymbol{r} = [x, y, z, 1]^{\boldsymbol{T}}$, $\boldsymbol{P}_m$ and $\boldsymbol{Q}_{lmt}$ are called major basis vectors and minor basis vectors, respectively. $\boldsymbol{P}_m$ is used to control the type of the periodic surface model, and $\boldsymbol{Q}_{lmt}$ is for fiber shape adjustment such as curvature. ψ_0 is an iso-surface value in [0,1]. An extended explanation of the parameters in Eq. [1] can be found in (22). In this study, a specific rod periodic surface model which is introduced 'rotation' and 'translation' is proposed to generate curved cylindrical fibers based on Eq. [1],

$$f(\boldsymbol{r}) = 4cos\left(2\pi(\boldsymbol{RT}P_1)^T\boldsymbol{r}\right) + ucos\left(2\pi f(\boldsymbol{RT}Q_1)^T\boldsymbol{r})\right) + 4cos\left(2\pi(\boldsymbol{RT}P_2)^T\boldsymbol{r})\right) + 4cos\left(2\pi(\boldsymbol{RT}P_3)^T\boldsymbol{r})\right) - 4cos\left(\pi(1-S_r)\right) + 1 = 0 \quad [2]$$

Where, $\boldsymbol{R} = [R_1, R_2, R_3, R_4]$ and $\boldsymbol{T} = [T_1, T_2, T_3, T_4]$ are the rotation and translation matrixes defined in (22). $R_1 = [cos(\theta)cos(\omega) - sin(\theta)sin(\varphi)sin(\omega), cos(\theta)sin(\omega) + cos(\omega)sin(\varphi)sin(\theta), -cos(\varphi)sin(\theta), 0]^T$, $R_2 = [-cos(\varphi)sin(\omega), cos(\varphi)cos(\omega), sin(\varphi), 0]^T$, $R_3 = [cos(\omega)sin(\theta) + cos(\theta)sin(\varphi)sin(\omega), sin(\theta)sin(\omega) - cos(\theta)cos(\omega)sin(\varphi), 0]^T$, $R_4 = [0, 0, 0, 1]^T$. $T_1 = [1, 0, 0, -t_1]^T$, $T_2 = [0, 1, 0, -t_2]^T$, $T_3 = [0, 0, 1, -t_3]^T$, $T_4 = [0, 0, 0, 1]^T$. φ, θ, and ω are three rotation angles about the x-, y-, and z-axes, and t_1, t_2, and t_3 are three translation scales in the x-y, y-z, and x-z planes. The selected parameter values and ranges in the present research are listed in TABLE I. The value of ω, t_1, t_2, and t_3 are all uniformly chosen from the given ranges. In addition, u and f are utilized to adjust the fiber curvature magnitude and frequency of the carbon fiber. The rotation angles around the x- and y-axes are set to 0 in previous reconstruction work (22), which means all the fibers are generated parallel to the x-y plane, namely, no Through-Plane (TP) oriented fibers are generated. Therefore, the reconstruction loses access to anisotropy, which can be realized by adjusting fiber orientation. In current work, instead of using a uniform distribution, a distribution density function (PDF) $P(\theta)$ proposed by Stoyan et al. (23) is first combined with Eq. [2] to control the probability of the rotation angle θ,

$$P(\theta) = \frac{1}{2}\frac{\beta cos\theta}{(1 + (\beta^2 - 1)sin^2\theta)^{\frac{3}{2}}} \quad [3]$$

In Eq. [3], β is called anisotropy parameter. $\beta = 0$ means that all the carbon fibers are aligning parallel to the TP direction. Increasing β results in more and more fibers oriented in the In-Plane (IP) direction. It should be mentioned that the periodic surface model presented in Eq. [2] is dimensionless and confined within a cubic domain with $x, y, z \in [0,1]$. Thus, a parameter S_r is utilized for subsequent full-dimensional scaling. S_r signifies the ratio between the anticipated fiber diameter (d) and the scaling factor (D). The determination of D entails a consideration of the largest dimension of the expected GDL.

TABLE I. Key parameters used in the periodic surface model.

Parameters	Value/Value range
φ	0
θ	$[-\pi/2, \pi/2]$
ω	$[-\pi, \pi]$
t_1	$[0, 1]$ (22)
t_2	$[0, 1]$ (22)
t_3	$[-0.491, -0.216]$
u	$[0, 0.6]$
f	$[0, 2.7]$
$[P_1, P_2, P_3, Q_1]$	$[[0,1,0,0]^T, [0,0,1,0]^T, [0,0,0,0]^T, [1,0,0,0]^T]$ in x-y plane (22)

Pore size distribution

Capillary pressure is an important parameter that can be used to assess the drainage capacity of a porous media, which is usually approximately predicted using $P_c = -2\sigma cos\phi/r$. Here, σ represents the surface tension force, ϕ denotes the contact angle, and

r corresponds to the pore size radii. Therefore, the fluid transport properties of a GDL are significantly influenced by its Pore Size Distribution (PSD).

The PSD of the reconstructed GDLs is analyzed by utilizing the *local_thickness* and *pore_size_distribution* functions available in the open-source software PoreSpy (24). Xu et al. (25) adopted a 2D image-based method to calculate the PSD, in which the pore area in each binary image is fully overlapped using circles with different radii. However, this method ignores the pore connection between adjacent images, which results in a maximum pore diameter of more than 100 μm in the range of pore diameters achieved. Considering a typical GDL thickness in the range of 180-300 μm, this value appears to be an overestimation. In this research, the generated stereolithography GDL geometry file is transformed into a 3D binary voxel volume using ImageJ software. The *local_thickness* function replaces the label of each pore voxel with the radii of the largest sphere that would overlap it. Furthermore, the PSD is calculated from the histogram of radii in the relabeled voxel volume by the *pore_size_distribution*.

Results and discussion

Reconstruction parameters

In the following reconstructions, the required GDL fiber diameter, domain size, and porosity are obtained from an image-based GDL - Freudenberg H2315 (26), shown in Fig. 1. The experimental GDL was calculated in Paraview software, with a domain size of $500\ \mu m \times 500\ \mu m \times 117\ \mu m$ and a bulk porosity of approximate 0.7, which is close to the value of observed for this type of GDL by Zhang et al. (13), i.e., 0.69. The GDL was sliced along the z-direction with a slicing resolution of 1 μm. The slice sequence was imported to ImageJ, and the TP porosity distribution and the fiber diameter were obtained, as shown in Fig. 1(c) and Fig. 1(d). The average fiber diameter is around 9 μm based on 178 random samples. The average porosity is also calculated based on a series of the TP local porosity, about 0.698, which is close to the bulk porosity.

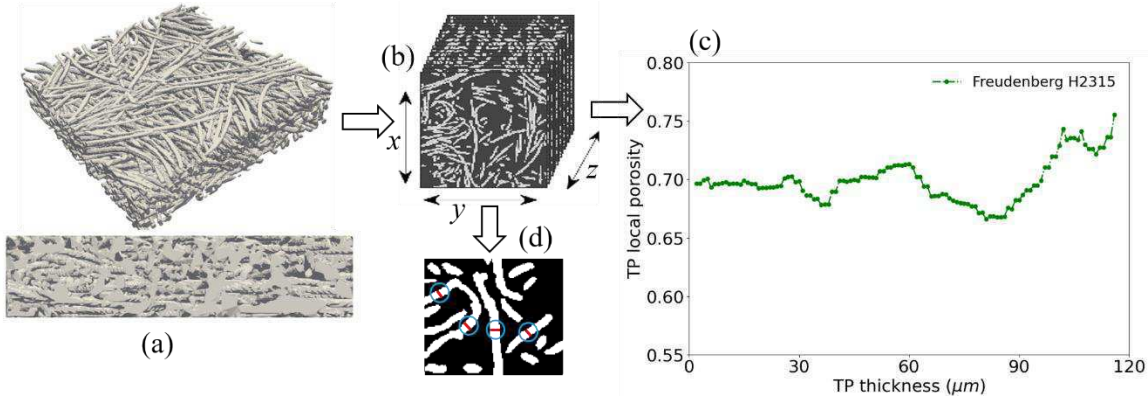

Figure 1. (a) Side views of experimental image-based reconstruction of the Freudenberg H2315 GDL. (b) IP cross-section slice sequence of the GDL along the TP direction with a slicing resolution of 1 μm. (c) TP local porosity distribution along the TP direction (thickness direction). (d) The determination of GDL fiber diameter through the utilization of pixel measurements in a series of binary images, where the white shade indicates the fiber slice.

In addition, the Freudenberg H2315 GDL exhibits several apparent features: (1) The fibers display varying degrees of curvature, with part of them showing slight bends rather than being perfectly straight; (2) The fibers are predominantly oriented in the IP direction, while some exist in the TP orientation with different angles with respect to the IP direction. (3) The side view in Fig. 1(a) reveals that the presence of binder connecting the fibers; (4) The experimental GDL contains sufficiently short fibers, allowing for a wide range of variation in GDL fiber length. Therefore, these features are incorporated into the GDL reconstruction in the present study, and their influence on the GDL properties is evaluated by comparing them with the experimental GDL through the PSD and TP local porosity analysis.

Fiber curvature

In this section, the value of $[P_1, P_2, P_3, Q_1]$ that corresponds to the x-y plane is selected and the parameter θ is fixed with 0, which means all the fibers are aligned in the x-y plane. To investigate the impact of fiber curvature, both straight-fiber and curved-fiber GDLs are generated using the periodic surface model. Both u and f are set to 0 for straight-fiber GDLs, whereas for curved-fiber GDLs, three ranges of u, i.e., $u \in [0.0, 0.2]$, $u \in [0.2, 0.4]$, and $u \in [0.4, 0.6]$, together with the same range for $f \in [0.7, 2.7]$ are utilized. Furthermore, the TP porosity distribution of the experimental GDL is applied to the reconstruction, which will be further discussed in the subsequent section. To increase the generality of the reconstructed GDLs, the reconstruction procedure of each type of GDL is performed five times, resulting in the generation of five 'random' GDLs for each fiber curvature range. The representative geometries of the four types of GDLs are illustrated in Fig. 2(a-d). As the range of u increases, an increasing number of curved fibers are observed within the GDLs.

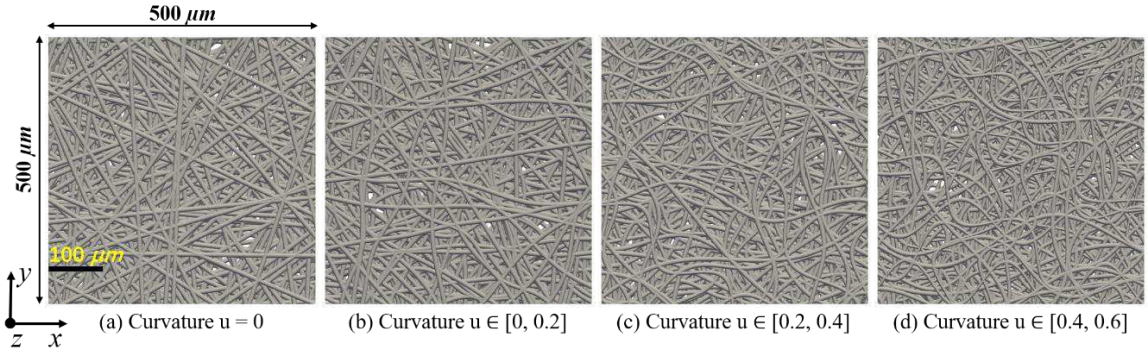

Figure 2. Top views of four reconstructed Gas Diffusion Layers (GDLs) exhibiting varying ranges of fiber curvature.

The TP local porosity distribution for these four representatives is also analyzed and compared with that of the experimental GDL, as shown in Fig. 3(a). The four stochastic GDLs exhibit a comparable TP porosity distribution, showing a similar major trend as the H2315 GDL. They all display a similar oscillation around the experimental values due to the cylindrical shape of the fibers and the decreased connection area between adjacent fiber layers. In addition, the mean PDF of the PSD for each GDL type in Fig. 3(b) is determined by analyzing the individual PSD of five GDL samples in each category which is shown in the Appendix (see Fig. A(a-d)). In comparison with the experimental GDL, it is found that find the GDL with a fiber curvature of u∈[0, 0.2] gives closer PDF results. The straight-

fiber GDL shows a similar trend to that of GDL with u∈[0.0, 0.2]. However, it leads to an overprediction in the regime of PDF peak. Moreover, the GDL with u∈[0.2, 0.4] has smaller mean value in the pore diameter range of 10-30 μm. The GDL with u∈[0.4, 0.6] is observed an overprediction before the PDF peak regime and underestimation after the peak. The results indicate that a higher fiber curvature tends to create smaller pores. In this study, the fiber curvature u∈[0.0, 0.2] is selected for further investigation.

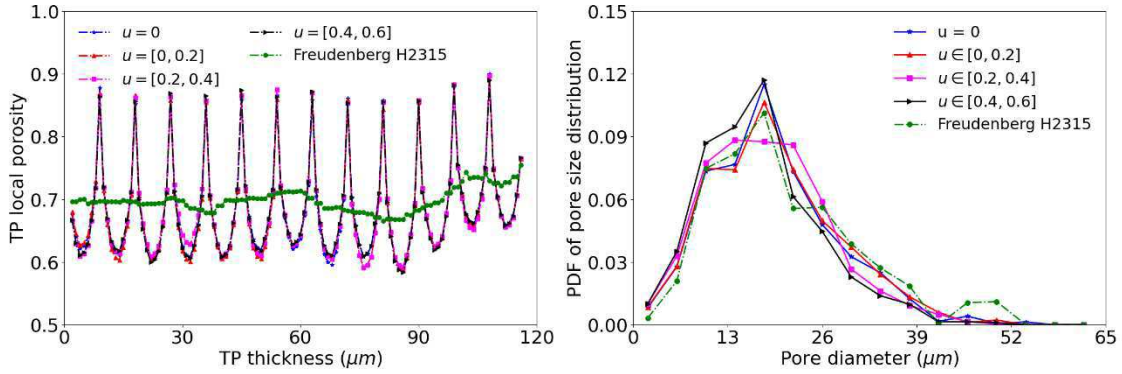

(a) (b)

Figure 3. Comparison among the four types of GDLs as well as the experimental GDL. (a) The TP local porosity of four representative GDLs with different fiber curvature. The oscillation around the experimental values results from the cylindrical shape of the fibers and the decreased connection area between adjacent fiber layers. (b) The mean PDF of the PSD for four types of GDLs.

TP porosity and bulk porosity

Porosity is a commonly used parameter in the GDL reconstruction process, most of the GDL reconstructions use the bulk porosity (13, 27-29) while only a few studies include the TP porosity distribution (17, 30). Typically, the TP porosity distribution and bulk porosity are introduced by generating GDL fibers with or without layer-by-layer stacking strategies. In current work, three fiber stacking strategies are presented, i.e., layer-by-layer stacking with the TP porosity, layer-by-layer stacking without the TP porosity, and random stacking with the bulk porosity.

The reconstructed GDLs have a thickness of 117 μm, the first two layer-by-layer methods equally divide the GDL into 13 fiber layers along the thickness direction, where each layer has a measurement of 9 μm. As long as the TP porosity is adopted, the locally averaged porosity values in the corresponding 13 layers of the experimental GDL are utilized. That means each layer is reconstructed with fibers until the target layer porosity is satisfied. In contrast, the method of layer-by-layer stacking without the TP porosity randomly distributes fibers in these separated layers until the expected bulk porosity is reached. In the strategy of random stacking with bulk porosity, layer division is not considered, and the fiber locations are randomly selected in the given range. Figure 4 shows the side views coming from three representative GDLs for the three stacking methods. It is clear to see that the first two fiber stacking methods exhibit clear and strict classification between adjacent layers, while the last one illustrates strong interconnection among different fibers in both the TP and IP directions. The influence of these options on the GDL

PSD is going to be studied. Five GDLs are generated using every strategy, with each of their PSD analyses shown in the Appendix (see Fig. B(a-c)).

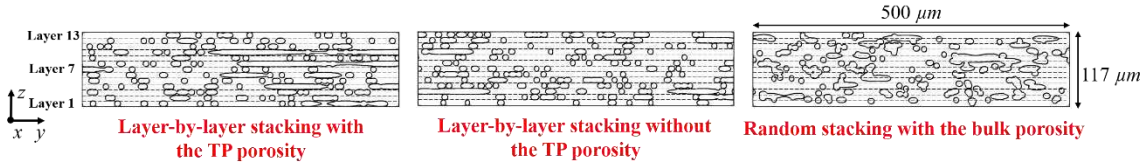

Figure 4. The *y-z* plane slices of three reconstructed GDLs with different layer stacking strategies.

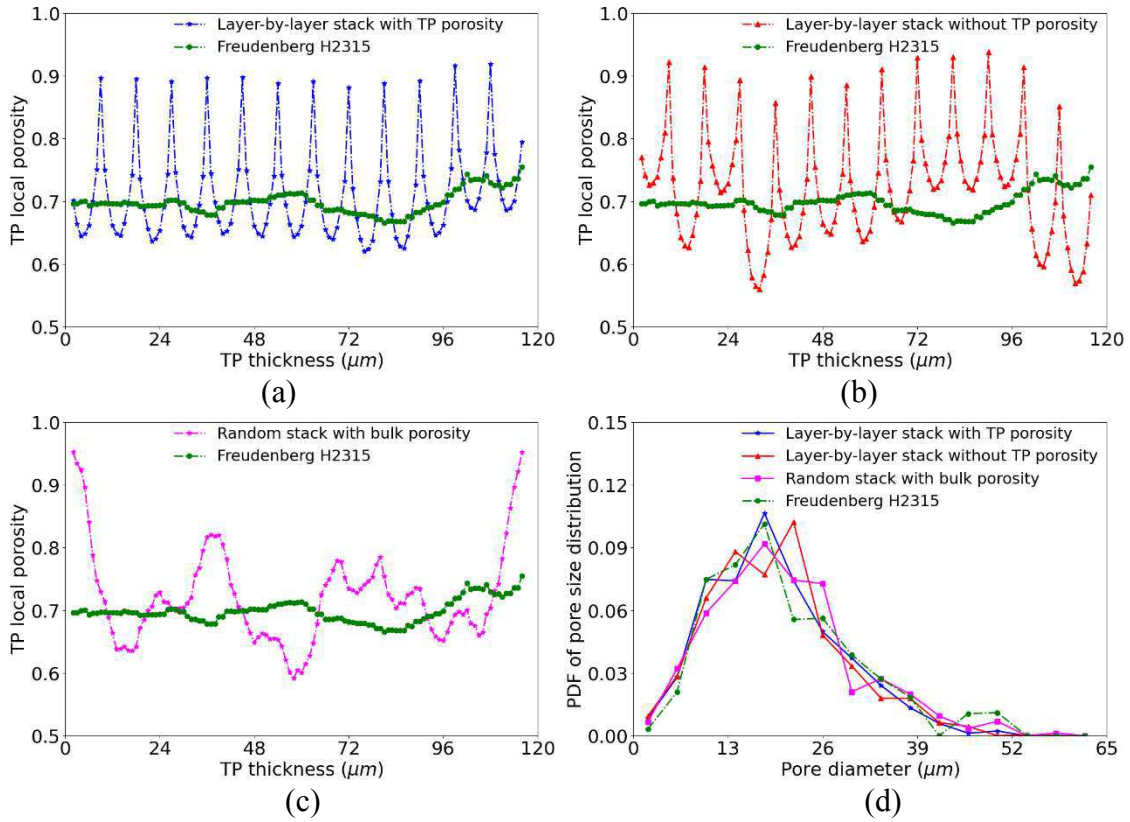

Figure 5. (a-c) The TP local porosity for the representative GDLs of three kinds of GDLs. The oscillation around the experimental values in (a-b) results from the cylindrical shape of the fibers and the decreased connection area between adjacent fiber layers. (d) PDF analysis of the PSD for three GDLs with various layer arrangements as well as the experimental GDL.

Figure 5(a-c) display the TP local porosity distribution of three representative GDLs. It is found that their TP local porosity all oscillates around that of the experimental GDL. Compared with the last stacking strategy in Fig. 4, involving random stacking with bulk porosity, the former two stacking strategies result in stronger and sharp oscillations. This distinction comes from the varying interconnection and overlaps between adjacent layers. However, the GDL representation using the layer-by-layer stacking method shows a similar major trend to the experimental GDL (see Fig. 5(a)). On the contrary, the TP porosity distribution in the GDL is random when the bulk porosity is adopted, in Fig. 5(b-c). Moreover, the last representative GDL in Fig. 5(c) has a smoother variation of the TP porosity. The mean PDF profiles in Fig. 5(d) show that the strategy of layer-by-layer

stacking considering the TP porosity yields a reconstruction that is closer to the experimental one, followed by random stacking using bulk porosity. However, the case of layer-by-layer stacking without the TP porosity results in the reconstructions far from the experimental GDL.

Anisotropy

The GDL structure's anisotropic property is affected by the fiber orientation, for example, along the IP or TP direction. A few previous studies have considered this factor (13, 27). To the best knowledge of the authors, there is no study considering both fiber curvature and anisotropy. Thus, an orientation-control PDF function is introduced to the periodic surface model, see Eq. [3], to investigate its effect on GDL properties. It should be mentioned that only the bulk porosity is utilized in this part. Simultaneous consideration of the TP porosity and anisotropy would be involved in future work. The anisotropic parameter β is utilized to adjust the probability of the fiber orientation angle. The PDF profiles of the rotation angle with six values of β are shown in Fig. 6. One could see that a larger value of β leads to an increased concentration of the angle around $\pi/2$.

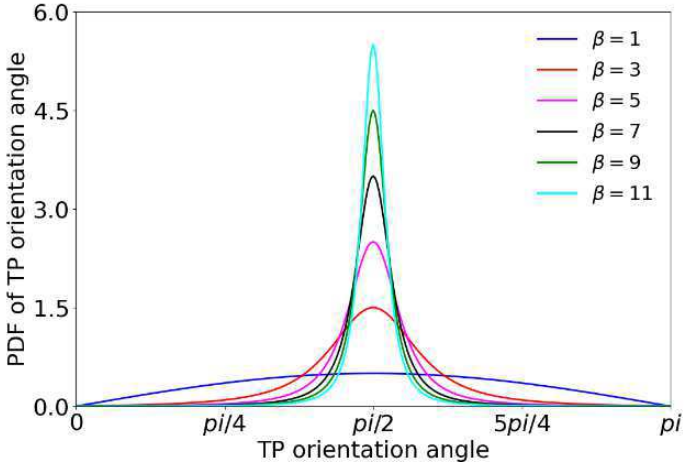

Figure 6. The PDF of the TP orientation angle in different value of β, i.e., 1, 3, 5, 7, 9, 11.

In this study, three GDLs are reconstructed with the values of β set to 1, 5, and 9, and their corresponding representative configurations are shown in Fig. 7. By increasing β, a greater alignment of fibers parallel to the IP direction can be achieved, which also could be seen from the slice of each representative GDL. The TP porosity distribution of the three GDLs are displayed in Fig. 8(a). The results show that the local porosity of three GDLs vary randomly without major trends to the experimental one. However, the smaller β, the smaller oscillation magnitude of the local porosity. Five GDLs in each of these three types are generated, and the individual GDL PSD analysis is shown in Appendix Fig. C(a-c). Based on the five cases in each kind of GDL, the mean PDF profiles of the PSD are calculated and shown in Fig. 8(b). The GDLs with $\beta = 1$ have an underestimation of the PDF located in the range of 10-20 μm, and an overprediction in the range of 20-40 μm. The GDLs involving $\beta = 5$ give a better matched PDF of the PSD to the experimental one.

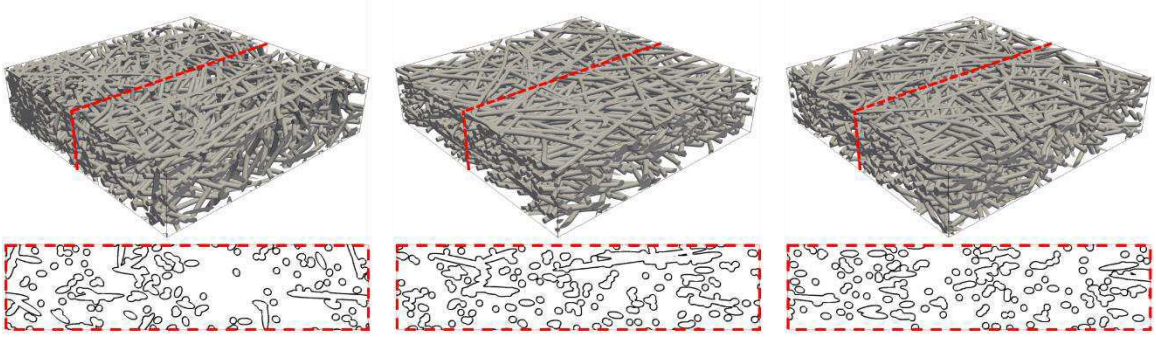

$\beta = 1$ $\beta = 5$ $\beta = 9$

Figure 7. The GDL configurations using different value of β: 1, 5, and 9.

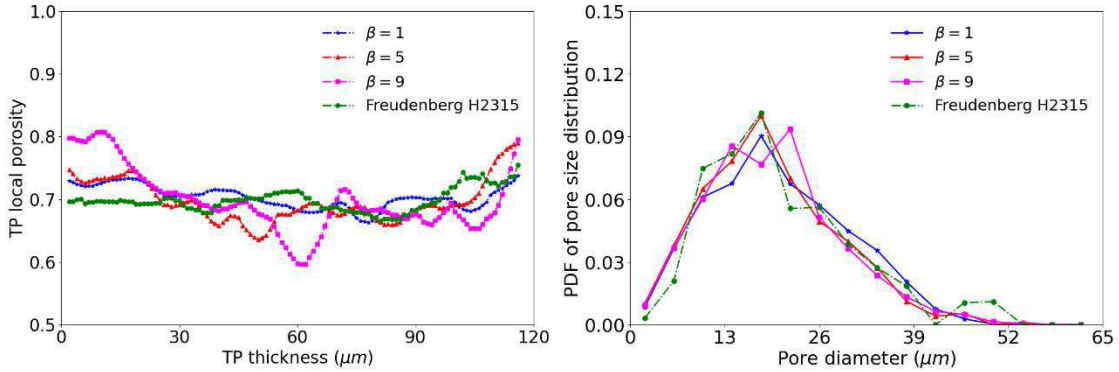

(a) (b)

Figure 8. (a) The comparison of the TP local porosity among three representative GDLs and the experimental GDL; (b) The mean PDF analysis of the PSD for three types of GDLs as well as the experimental GDL with β set to 1, 5, and 9.

Conclusion

The bulk porosity, through-plane porosity, fiber diameter, and domain size of an experimental GDL structure are obtained for further stochastic reconstructions. A rod periodic surface model has been applied to generate GDLs with different fiber curvature and fiber layer stacking strategies. Moreover, a specific rotation angle distribution function is introduced and combined with the periodic surface model to include anisotropy in the reconstruction. To minimize the occurrence of accidental cases, five GDLs are generated in each type of GDL. The averaged PSD values of these GDLs are used in further comparison among different kinds of GDL reconstructions. The influence of three structural features on the TP local porosity and 3D PSD are analyzed. The representation of each generated GDL type is compared with the experimental GDL. The results show that using bulk porosity as an ending target in reconstructions leads to the random fluctuation of the TP local porosity, and the utilization of anisotropy can decrease the oscillation magnitude. In addition to the individual PSD analysis of each reconstructed GDL, the mean PDF of the PSD for each type of GDL is also calculated and compared with the PDF of the experimental GDL. The results show that considering a reasonable fiber curvature and anisotropy could make the reconstruction closer to the real one in terms of PSD.

Future work

Reconstructing GDLs has incorporated experimental features to enhance realism, but further improvements are still needed. One notable advancement is the layer-by-layer stacking strategy utilizing TP porosity, which provides increased control in the stochastic process. However, this strategy also introduces noticeable oscillation. To address this, a promising approach is to consider both TP porosity distribution and anisotropy, which can mitigate fluctuations while requiring a more complex implementation. In addition, the reconstruction of binder and polytetrafluoroethylene is also crucial for a wider GDL analysis. On the other hand, even if the more similar GDL PSD property, the other properties also need to be estimated such as tortuosity, permeability, and thermal and electric conductivity. The water behavior inside the GDL is still unknown. Numerical studies of two-phase flow need to be conducted to investigate the phenomenon in both stochastic and physical GDLs.

Acknowledgments

The authors wish to thank Dr. Eugen Hoppe for constructing a stereolithography file of the porous material used in this study. D. Yang sincerely acknowledges the Chinese Scholarship Council, grant number: 202006070174.

References

1. A. Parekh, *Front. Energy Res.*, **10**, 956132 (2022).
2. L. Zhao, H. Chen, and T. Zhang, *Appl. Energy*, **327**, 120058 (2022).
3. C. Zhang, Y. Zhang, L. Wang, X. Deng, Y. Liu, and J. Zhang, *Renewable Sustainable Energy Rev.*, **182**, 113369 (2023).
4. P. C. Okonkwo, and O. Clement, *Int. J. Energy Res.*, **45**(3), 3780 (2021).
5. M. Andersson S. Beale, M. Espinoza, Z. Wu, and W. Lehnert, *Appl. Energy*, **180**, 757 (2016).
6. Y. Pan, H. Wang, and N. P. Brandon, *J. Power Sources*, **513**, 230560 (2021).
7. Y. Yang, X. Zhou, B. Li, and C. Zhang, *Int. J. Hydrog. Energy*, **46**(5), 4259 (2021).
8. H. Ostadi, P. Rama, Y. Liu, R. Chen, X. X. Zhang, and K. Jiang, *J. Membr. Sci.*, **351**(1-2), 69 (2010).
9. M. Andisheh-Tadbir, F. P. Orfino, and E. Kjeang. *J. Power Sources*, **310**, 61 (2016).
10. J. P. James, H. W. Choi, and J. G. Pharoah, *Int. J. Hydrog. Energy*, **37**(23), 18216 (2012).
11. S. Odaya, R. K. Phillips, Y. Sharma, J. Bellerive, A. B. Phillion, and M. Hoorfar, *Electrochim. Acta*, **152**, 464 (2015).
12. S. Simaafrookhteh, R. Taherian, and M. Shakeri, *J. Electrochem. Soc.*, **166**(7), F3287 (2019).
13. H. Zhang, L. Zhu, H. B. Harandi, K. Duan, R. Zeis, P. C. Sui, and P. Y. A. Chuang, *Energy Convers. Manag.*, **241**, 114293 (2021).
14. X. Zhou, Z. Niu, Z. Bao, J. Wang, Z. Liu, Y. Yin, Q. Du, and K. Jiao, *J. Power Sources*, **437**, 226933 (2019).

15. I.V. Zenyuk, D.Y. Parkinson, G. Hwang, and A.Z. Weber, *Electrochem. commun.*, **53**, 24 (2015).
16. T. Lai, and Z. Qu, *Energy*, **271**, 126920 (2023).
17. X. Shangguan, Y. Li, Y. Qin, S. Cao, J. Zhang, and Y. Yin, *Electrochim. Acta*, **371**, 137814 (2021).
18. L. Zhu, H. Zhang, L. Xiao, A. Bazylak, X. Gao, and P. C. Sui, *J. Power Sources*, **496**, 229822 (2021).
19. D. Niblett, A. Mularczyk, V. Niasar, J. Eller, and S. Holmes, *J. Power Sources*, **471**, 228427 (2020).
20. D. Yang, H. Garg, and M. Andersson, *Int. J. Hydrog. Energy*, **48**(41), 15677 (2023).
21. Y. Wang, *Comput. Aided Des.*, **39**(3), 179 (2007).
22. W. Huang, S. Didari, Y. Wang, and T. A. L. Harris, *Eng. Comput.*, **32**(1), 7 (2015).
23. D. Stoyan, J. Mecke, and S. Pohlmann. *Statistics: theor. appl. stat.*, **11**(2), 281 (1980).
24. J. Gostick, Z. A. Khan, T. G. Tranter, M. D. R. Kok, M. Agnaou, M. A. Sadeghi, R. Jervis, *J. Open Source Softw.*, **4**(37), 1296 (2019).
25. H. Xu, S. Nagashima, H. P. Nguyen, K. Kishita, F. Marone, F. N. Büchi, and J. Eller, *J. Power Sources*, **490**, 229492 (2021).
26. S. B. Beale, M. Andersson, N. Weber, H. Marschall, and W. Lehnert, *ECS Trans*., **98**(9), 305 (2020).
27. L. Xiao, Z. Yin, M. Bian, N. Bevilacqua, R. Zeis, J. Yuan, and P. C. Sui, *Int. J. Hydrog. Energy*, **47**(46), 20218 (2022).
28. Z. Bao, Y. Li, X. Zhou, F. Gao, Q. Du, and K. Jiao, *Int. J. Heat Mass Transf.*, **178**, 121608 (2021).
29. M. M. Daino, and , S. G. Kandlikar, *Int. J. Hydrog. Energy*, **37**(6), 5180 (2012).
30. Z. Niu, Y. Wang, K. Jiao, and J. Wu*, J. Electrochem. Soc.*, **165**(9), F613 (2018).

List of abbreviation

PEMFC	Proton Exchange Membrane Fuel Cell
GDL	Gas Diffusion Layer
PSD	Pore Size Distribution
TP	Through-Plane
IP	In-Plane
PDF	Probability Density Function

Appendix

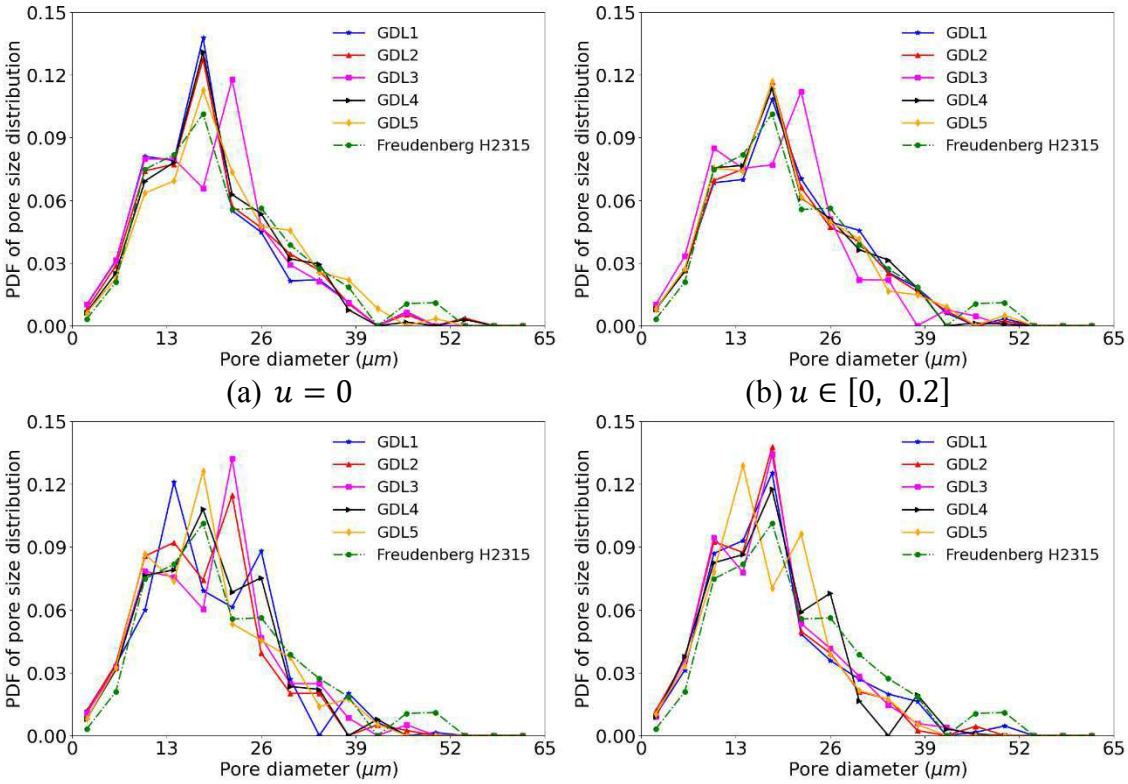

(a) $u = 0$ (b) $u \in [0,\ 0.2]$

(c) $u \in [0.2,\ 0.4]$ (d) $u \in [0.4,\ 0.6]$

Figure A. PDF of the PSD for each generated GDLs with different curvatures.

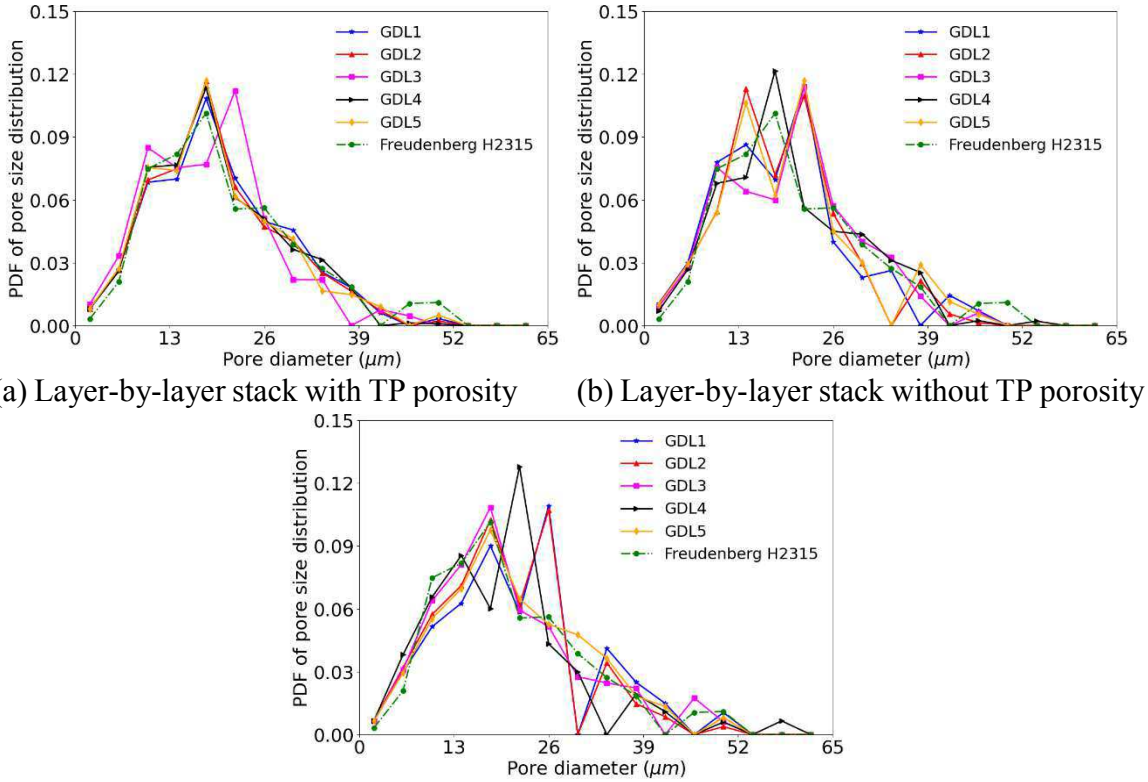

(a) Layer-by-layer stack with TP porosity (b) Layer-by-layer stack without TP porosity

(c) Random stack with bulk porosity

Figure B. PDF of the PSD for each generated GDLs with different layer stacking strategies.

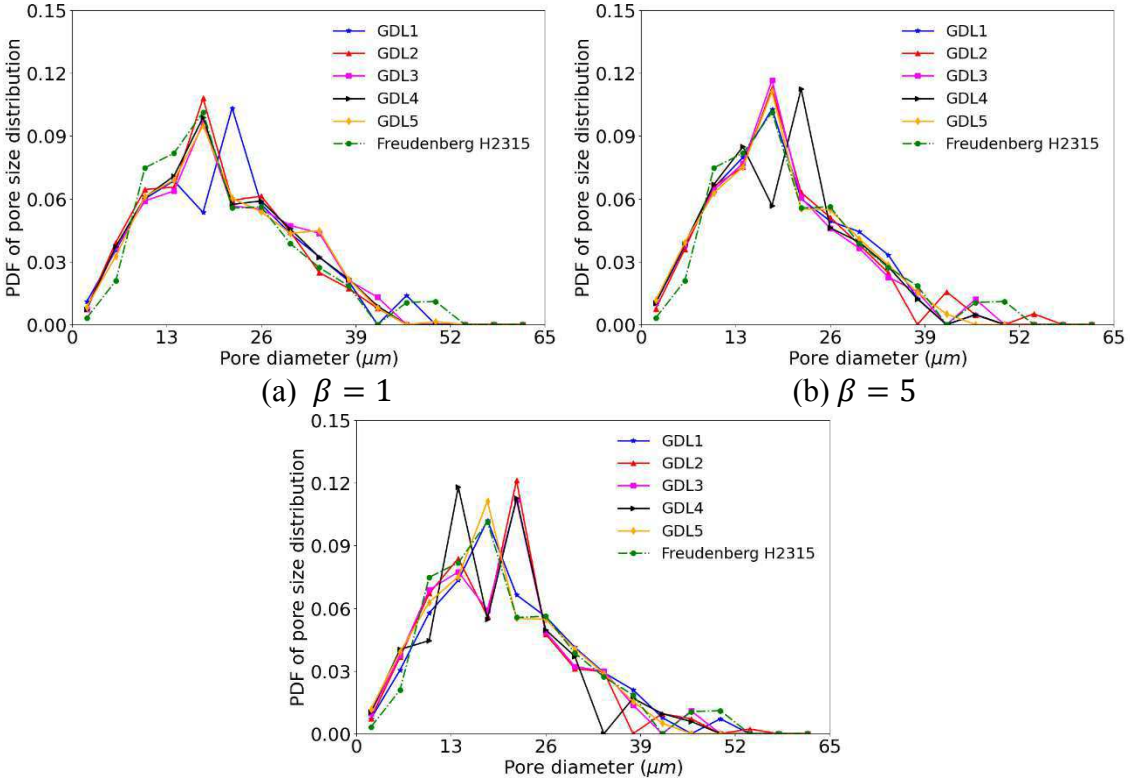

(a) $\beta = 1$ (b) $\beta = 5$

(c) $\beta = 9$

Figure C. PDF of the PSD for each generated GDLs with different anisotropy parameter.